Geophysical Journal International

Geophys. J. Int. (2018) **213,** 2161–2176
Advance Access publication 2018 March 09
GJI Marine geosciences and applied geophysics

doi: 10.1093/gji/ggy093

Uncertainty analysis of depth predictions from seismic reflection data using Bayesian statistics

Dimitrios G. Michelioudakis,[1] Richard W. Hobbs[1] and Camila C.S. Caiado[2]

[1]*Department of Earth Sciences, University of Durham, Durham* DH1 3LE*, UK. E-mail: dimitrios.michelioudakis@durham.ac.uk*
[2]*Department of Mathematical Sciences, University of Durham, Durham* DH1 3LE*, UK*

Accepted 2018 March 8. Received 2018 March 5; in original form 2017 July 4

SUMMARY

Estimating the depths of target horizons from seismic reflection data is an important task in exploration geophysics. To constrain these depths we need a reliable and accurate velocity model. Here, we build an optimum 2-D seismic reflection data processing flow focused on pre-stack deghosting filters and velocity model building and apply Bayesian methods, including Gaussian process emulation and Bayesian History Matching, to estimate the uncertainties of the depths of key horizons near the Deep Sea Drilling Project (DSDP) borehole 258 (DSDP-258) located in the Mentelle Basin, southwest of Australia, and compare the results with the drilled core from that well. Following this strategy, the tie between the modelled and observed depths from DSDP-258 core was in accordance with the $\pm 2\sigma$ posterior credibility intervals and predictions for depths to key horizons were made for the two new drill sites, adjacent to the existing borehole of the area. The probabilistic analysis allowed us to generate multiple realizations of pre-stack depth migrated images, these can be directly used to better constrain interpretation and identify potential risk at drill sites. The method will be applied to constrain the drilling targets for the upcoming International Ocean Discovery Program, leg 369.

Key words: Australia; Image processing; Probability distributions; Statistical methods.

1 INTRODUCTION

Velocity model building is a critical step in seismic reflection processing. An optimum velocity field can generate flat common image gathers (CIGs) and well-focused images in time or depth domain. Nevertheless, taking into account the noisy and band limited nature of the seismic reflection data and the ambiguity in the velocity estimation, the generated velocity field is only our best estimate of a set of possible velocity fields (Bickel 1990; Tieman 1994; Kosloff & Sudman 2002). Hence, all the calculated depths and the images produced are just our best approximation of the true subsurface.

Although incorporating anisotropic parameters (Thomsen 1986; Alkhalifah & Tsvankin 1995; Alkhalifah 1997) during the velocity analysis stage can assist to constrain better the depth results (Hawkins *et al.* 2001), the non-uniqueness of the velocity field still remains an open problem as different velocity fields can lead to nearly equally flat arrivals in CIG (Chitu *et al.* 2008). The problem is worse in the absence of any well log information, where the velocity field cannot be calibrated, rendering the final structural image only a sample among the most probable images, as an optimally focused image does not necessarily mean accuracy of depths (Al-Chalabi 1994, 2014).

Conventionally, the initial estimation of the reflection time and root mean square velocities (V_{rms}) for each geological layer is based on picking the local maxima on a semblance spectrum (Neidell & Taner 1971), computed from common mid-point (CMP) gathers. The ambiguity associated with the velocity model building is shown schematically in Fig. 1. The CMP gather is normal moveout (NMO) corrected with 3 slightly different velocity fields after 4.2 s two-way-time (TWT), but visually the reflection arrivals appear equally flat (Figs 1a and b). Earlier than 4.2 s, the maxima are less ambiguous to pick and the degree of precision of each picked value is higher. However, the velocity model building for deeper structures is compromised by the low depth to offset ratio and the attenuated frequency and amplitude content of the signal. This velocity–depth issue limits the sensitivity of residual moveout to velocity changes and indicates that the semblance spectrum as a tool lacks the resolution to provide us with a unique velocity model (Lines 1993). Tomographic inversion in the migrated domain for velocity estimation is inherently non - unique (Jones 2014) as it is trying to match the observed time values by choosing different combinations of depth (z) and slowness (s) values (Jones 2010). Multiple realizations of the same boundary can be created, all having slightly different pairs of z, s (Fig. 1c).

Attempts have been made to incorporate statistical information in seismic reflection data processing and perform uncertainty analysis for constraining velocities or depth results (Abrahamsen *et al.* 1991; Landa 1991; Chitu *et al.* 2008; Lewis *et al.* 2015;

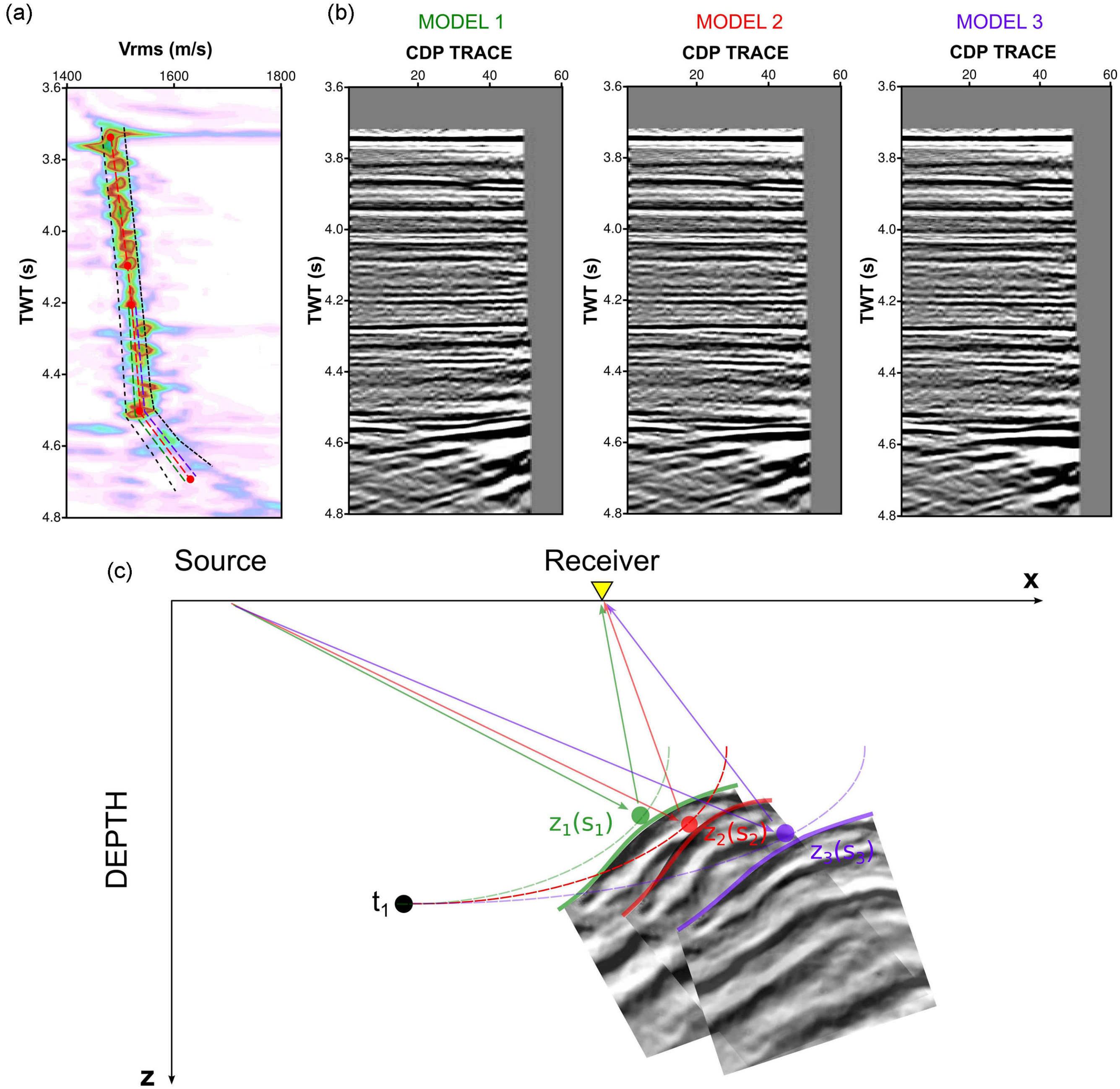

Figure 1. Uncertainty in velocity model building. (a) The semblance spectrum as a velocity estimation tool gives robust time–velocity picks for the shallow parts, but for later times the envelope of possible picked pairs (dashed black lines) becomes broader due to attenuation effects and poor depth to offset ratio. (b) The three velocity models (under colours red, purple and green), having differences only after 4.2 s TWT, result in equally flat gathers but can lead to different shapes and depths for the same horizons after pre-stack depth migration (pre-SDM). (c) Tomographic inversion in the depth migration domain preserves the observed invariant time (t_1) of an arrival by using different values of thickness (z) and slowness (s). As a consequence, the mapping from time to depth can result in slightly different realizations of the same boundary. (panel c, modified from Jones 2010, fig. 5.23).

Messud *et al.* 2017). The uncertain nature of the produced velocity field can be addressed by statistically analysing the given velocity model to quantify the uncertainty associated with each pick. In this paper, we will use high resolution 2-D seismic reflection data and develop a robust processing flow to effectively combine seismic analysis with Bayesian methods such as Gaussian Process emulation and Bayesian history matching (BHM), to quantify uncertainties in velocity models using a suite of algorithms called BRAINS [from Bayesian Regression Analysis In Seismology (Caiado *et al.* 2012)]. This paper can be considered as an extension of (Caiado *et al.* 2012), where a part of the methodology was initially outlined. However, this is the first time that the model with the statistical techniques are formalized and detailed. Also, to our knowledge, this is the first time that a combination of Gaussian Process emulators and BHM is implemented as part of a seismic processing flow.

The objective of this study is to estimate the uncertainties associated with the depths of drilling targets for the upcoming International Ocean Discovery Program project, leg 369 (Hobbs *et al.* 2017), located in Mentelle Basin, SW Australia (Fig. 2 a; Borissova 2002; Direen *et al.* 2007). In this area, stratigraphic information

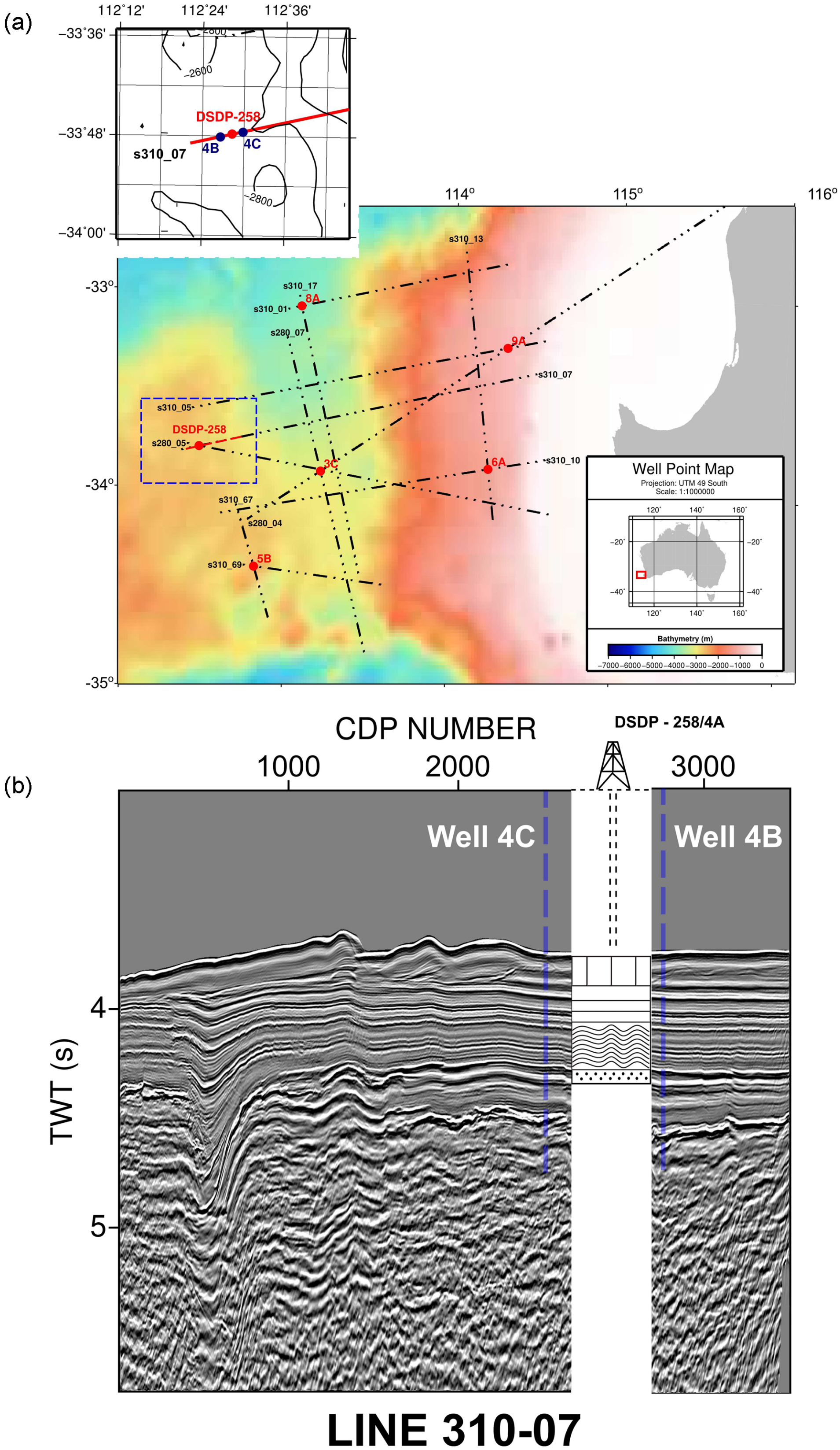

Figure 2. (a) Bathymetric map of Mentelle Basin. The positions of 2-D seismic lines (dashed black lines) and planned well locations (red circles) are shown. Red dashed line represent the segment reprocessed in this paper. Insert, the two new planned well positions adjacent to DSDP-258 are marked in blue (4B - 4C). (b) DSDP-258 borehole tied to ghost free Pre - Stack time migrated (preSTM) profile S310-07. In the lithological interpretation: vertical hatching carbonate oozes; horizontal hatching chalks; wavy hatching black shales; black stipples glauconitic sands. Blue dashed lines intersecting profile S310-07, indicate the positions of Wells 4C, 4B respectively.

is available from the Deep Sea Drilling Project (DSDP) borehole 258, which penetrated a series of carbonate oozes, limestones, black shales and sands (Davies *et al.* 1974; Fig. 2b), deposited during the Cretaceous Hothouse period (90–70 Ma). Part of the sedimentary sequence may contain evidence for sudden decrease in atmospheric CO_2 concentrations with associated periods of glaciation (Kuypers *et al.* 1999). By drilling and recovering samples from targeted geological sequences, we can collect valuable information about the palaeotemperature regime, biotic records, ocean circulation and tectonic history of the region.

Poor core recovery and the lack of wireline sonic information from DSDP-258, means that the depth predictions of key horizons is based entirely on the velocity values inferred from surface seismic data. As the sensitivity of differential move out, during the velocity analysis stage using a semblance spectrum, is linked to the frequency content of the wavelet in pre-stack data (CMP gathers; Chen & Schuster 1999; Jones 2010), we opt to follow a complete seismic reflection processing flow with the main focus on improving the temporal resolution of the seismic data. This is achieved by eliminating the source and receiver ghost notches in the pre-stack domain using inverse deghosting filters. The latter approach allows us to perform pre-stack depth migration (pre-SDM) on the ghost free CMP gathers, and produce an image with optimum spatial resolution and focusing, which aids to better constrain the interpretation.

We use the probabilistically derived velocity estimates to retrieve the depth information for key boundaries, tied to borehole 258 and make predictions for the depths of drilling targets for the two planned wells 4B–4C, located adjacent to the borehole DSDP-258. Finally, as the probabilistic approach produces a posterior distribution of velocity values, we generate a set of velocity fields and produce different realizations of pre-SDM images for the line segment intersecting the planned wells (Figs 2a and b).

2 GEOLOGICAL SETTING OF THE STUDY AREA

The western and southern margins of Australia are defined as the two arms of a triple junction that formed during the final stages of the Gondwana breakup (Powell *et al.* 1988; Royer & Coffin 1992; Direen *et al.* 2007).

One of the most important geological features of that region is the Mentelle Basin (MB). It is a sparsely explored, deep water sedimentary basin, located between the Naturaliste Plateau and the southern part of the Western Australian Shelf. Seismic images based on early seismic surveys showed that Mentelle basin is elliptical in shape, with minor and major axes 200 km east-west and 220 km north-south, respectively. Its main depocenter, is believed to contain sediments from Cretaceous to Holocene which produce an interval of more than 3.0 s TWT on the seismic image (Borissova 2002; Bradshaw *et al.* 2003). These sediments are possibly underlain by older sediments from an earlier rifting event. The presence of a thick sedimentary sequence in the MB gives a petroleum potential similar to that of the southern Perth Basin (Borissova 2002).

The stratigraphic features of the MB are not delineated as this area is sparsely drilled. Nevertheless, the results of the borehole site (DSDP-258) in conjunction with newly processed and reprocessed seismic data from GA S280 and S310 surveys, Shell Petrel Development Survey and Geoscience Australia Continental Margins Surveys 18 (Sargent *et al.* 2011), allowed the division of the stratigraphy of MB into seismically derived tectonostratigraphic megasequences (Maloney *et al.* 2011).

3 METHODS

3.1 Gaussian process emulators for modelling seismic velocities

In the Bayesian framework, the expert's knowledge about the parameters that govern a system are represented using prior distributions, then the available data, in conjunction with a sampling model (likelihood function), are used to update our knowledge about these parameters (posterior distribution). In seismic reflection processing, we can use the observed amplitudes of reflection events in a CMP gather $\{A_{ij}\}$, offsets $\{X_j\}$, recorded traveltimes $\{T_{ij}^{(r)}\}$ and picked $\{V_{\mathrm{rms}_i}–T_{0_i}\}$ or derived $\{V_{\mathrm{int}.i}–T_{0_i}\}$ pairs as prior information and we aim to quantify the uncertainty of $\{\Delta T_{0_i}, \Delta V_{\mathrm{rms}_i}, V_{\mathrm{int}_i}, \Delta Z_i\}$ for the horizons of interest. BRAINS suite (Caiado *et al.* 2012) uses a combination of Bayesian methods, such as emulation and BHM, to quantify these uncertainties.

Our approach is based on a discrete subsurface model (Appendix A1), with a finite number i of geophysical layers and a given array of source (S_j)–receiver (R_j) pairs, $j = 1, ..., m$. These are symmetrically placed around a CMP, with X_j being the distance between S_j and R_j. For every X_j and hyperbolic event (layer) i, we have observed amplitude values A_{ij} and recorded time T_{ij}. Also, for each layer we can assign a zero-offset two–way traveltime T_{0_i}, its time increment ΔT_{0_i}, a root-mean-square velocity V_{rms_i} with its velocity increment $\Delta V_{\mathrm{rms}_i}$, an interval velocity V_{int_i} and a thickness ΔZ_i. Our model seeks to estimate variables $\{\Delta T_{0_i}, \Delta V_{\mathrm{rms}_i}, V_{\mathrm{int}_i}, \Delta Z_i\}$ and their relevant uncertainties, from observed data $\{A_{ij}, X_j, T_{ij}^{(r)}\}$, taking into account the prior information from picked $\{V_{\mathrm{rms}_i}, T_{0_i}\}$ or $\{V_{\mathrm{int}_i}, T_{0_i}\}$ pairs derived during the velocity analysis stage.

In the case of isotropic conditions, the recorded traveltime of a wave to propagate, under the ray assumption, from seismic source S_j to detector R_j, $T_{ij}^{(r)}$, can be expressed as

$$T_{ij}^{(r)} = \sqrt{T_{0_i}^2 + \left(\frac{X_j}{V_{\mathrm{rms}_i}}\right)^2} + \epsilon_{ij} + e_{ij}, \tag{1}$$

where ϵ_{ij} accounts for the model discrepancy due to propagating approximations and isotropic assumptions, e_{ij} corresponds to recording errors. Although recording error (e_{ij}), is present in a construction of a statistical model, as the observations are indirect and recorded with a finite accuracy, it is the model discrepancy term (ϵ_{ij}) that has a key role in our statistical representation. Model discrepancy integrates all the simplifications of physical laws, used to describe the model, with our incomplete knowledge about the system explored and represents our inability to build a model which depicts reality (Craig *et al.* 1997). Thus, by including the ϵ_{ij} term not only we address the potential issue of overfitting the model to the observed data (Andrianakis *et al.* 2015) but we also produce uncertainty estimations for the output variables of interest. As expressed in eq. (1), ϵ_{ij} term represents effects related with anisotropic wave propagation (ϵ, δ anisotropic parameters) and ray tracing approximation.

Typically, these error terms are ignored which results in the Dix equation (Dix 1955), where we can relate V_{rms_i} and V_{int_i} as

$$V_{\mathrm{int}_i} = \sqrt{\frac{T_{0_i} V_{\mathrm{rms}_i}^2 - T_{0_{i-1}} V_{\mathrm{rms}_{i-1}}^2}{T_{0_i} - T_{0_{i-1}}}} \tag{2}$$

and calculate the thickness ΔZ_i of each layer as

$$\Delta Z_i = \frac{V_{\mathrm{int}_i} \Delta T_{0_i}}{2}. \tag{3}$$

Eqs (2) and (3) are based on the hyperbolic approximation of the recorded traveltime. Including the error terms in eq. (1) allows a more robust approach, which is not restricted to hyperbolic assumptions but can express more complex models for incorporating recorded traveltime from seismic rays which follow a non-normal trajectory. We use the above equations to construct a Gaussian Process (GP) model. A GP can be thought as the generalization of the univariate Gaussian probability distribution and formally is defined as 'a collection of random variables with any finite number of which having a joint Gaussian distribution' (Rasmussen & Williams 2006). They are well established models, applied in a variety of spatial and temporal problems (Ripley 1991) including geostatistics (Matheron 1973; Journel & Huijbregts 1978) and Kalman filters (Ko & Fox 2009). A GP is fully defined by its mean, $m(a)$ and covariance $k(a, a')$ functions with a, a' representing samples from the random vector.

In this paper we will use the Gaussian Process emulators. An emulator is defined as a stochastic belief specification, which expresses probabilistic judgements for a deterministic function $f(a)$ (Craig *et al.* 1997; O'Hagan 2006; Vernon *et al.* 2010; Caiado & Goldstein 2015). Commonly, they are expressed in the following form:

$$f_h(a) = \sum \beta_{hj} g_{hj}(a) + u_h(a), \tag{4}$$

where a is input value, β_{hj} unknown scalars, $g_{hj}(a)$, known deterministic functions and $u_h(a)$ is a stochastic process, normally a GP with zero mean and a square exponential covariance function. Index h represents the output variable. As a result, in eq. (4) we can incorporate our beliefs and the uncertainties about each variable of the system explored.

In our statistical analysis, we use two emulators for uncertainty quantification. First, a local (1-D) emulator (Appendix A1), where we make the assumption that a set of traveltimes related to a given horizon in a single CMP can be approximated as a sample of a continuous function with a hyperbolic trend. If any finite set of traveltimes from this hyperbolic curve is believed to follow a multivariate Gaussian distribution, we can assume that the recorded traveltime curve is a GP with respect to offset x

$$\mathcal{T}_i^{(r)}(x)|\Delta T_{0_{(1,\ldots i)}}, \Delta V_{\mathrm{rms}_{(1,\ldots,i)}} \sim \mathcal{GP}(m_{t_i}(x), k_i(x, x')) \tag{5}$$

or expressed in a form consistent to eq. (1) as

$$\mathcal{T}_i^{(r)}(x) = (t_{0_i}^2 + x^2 \upsilon_{\mathrm{rms}_i}^{-2})^{1/2} + u_i(x). \tag{6}$$

The first term of the right-hand side represents the mean function $m_{t_i}(x)$ and the second term a stationary stochastic process with zero mean and a square exponential covariance functions $k_{t_i}(x, x')$, with the mean and covariance functions given below:

$$m_{t_i}(x) = (t_{0_i}^2 + x^2 \upsilon_{\mathrm{rms}_i}^{-2})^{1/2} \tag{7}$$

$$k_{t_i}(x, x') = \sigma_{n_i} + \sigma_{s_i} exp\left(-\frac{(x - x')^2}{d_i}\right). \tag{7}$$

The terms x and x' define two random points from the offset space within a single CMP. Comparing eq. (1) with expression (7) we can see that the hyperbolic trend of traveltime equation is stored under the mean function $m_{t_i}(x)$ and the error terms ϵ_{ij}, e_{ij} are stored under the noise parameters σ_{n_i}, σ_{s_i} of the covariance function. The parameter d_i represents the length-scale of the function and defines how far the x, x' values should be to become uncorrelated. The covariance function, can be adjusted to specific applications by correctly tuning its hyperparameters (σ_{n_i}, σ_{s_i}, d_i). As our prior knowledge about their appropriate values reflects our knowledge about the system, they can be treated as constants that need to be set manually or derived from an optimization process using the training data (Rasmussen & Williams 2006). In our case, the training data can be thought of as the set of prior $T_{0_i} - V_{\mathrm{rms}_i}$, $T_{0_i} - V_{\mathrm{int}_i}$ pairs picked during the velocity analysis stage. Based on the velocity analysis interval (spacing between two consecutive picked pairs), the picked values and also their variability along the picked velocity layer, we can manually calibrate accordingly, the noise, scale and length parameters of the covariance function and provide starting points for their values. Subsequently, the parameters are refined using a gradient search to find a local maximum in the likelihood and retrieve values in an area of high probability. Eqs (5)–(7) can be formulated analogously for linking $\mathcal{T}_i^{(r)}$ with V_{int_i} and ΔZ_i, rendering the Bayesian model multidimensional.

Second, a 2-D emulator expands the 1-D uncertainty estimation into a 2-D multigather representation by assuming that the variables ΔT_{0_i}, $\Delta V_{\mathrm{rms}_i}$, V_{int_i} and ΔZ_i, for every geophysical boundary, follow a GP over the CMP positions (x_c) along a profile (Appendix A2). The latter, is used to constrain the intergather areas and produce estimates in regions where we do not have available prior pick pairs.

3.2 Bayesian History Matching for model space reduction

In order to perform model calibration and reduce the parameter input space we use the approach known as BHM (Craig *et al.* 1997; Vernon *et al.* 2010). BHM is an established method and combined with emulation techniques has been tested successfully in a variety of different scientific disciplines such as reservoir modelling (Craig *et al.* 1997; Cumming & Goldstein 2009) climate modelling (Caiado & Goldstein 2015) and galaxy formation modelling (Vernon *et al.* 2010). BHM should not be confused with the term History Matching widely used in the oil industry, as in the latter case, we are trying to match empirical data, such as production rates and observed pressure from well logs, with a complex model (normally called simulator) that is assumed to represent part of the subsurface (reservoir), where the parameters that govern the model do not include any uncertainty estimation. On the contrary through the process of BHM, all the possible models that can match our observed data are identified (Vernon *et al.* 2010). Following the same notation as in eq. (4), in BHM, we aim to identify and iteratively discard input values, a, of the parameter space for which the evaluation of a function (emulator) $f_h(a)$ is not likely to provide a good match to the observed data L. The parts of parameter space that are discarded are called implausible and the process of reducing the space is accomplished using the probabilistic criterion of implausibility $I_h(a)$ (Craig *et al.* 1997; Vernon *et al.* 2010). The general definition of Implausibility is given below.

Definition 1. Implausibility

For a given choice of input value a with modelled output $f_h(a)$, observation vector L_h and taking into account all the variances present in the system $\mathrm{Var}_h(\mathrm{system})$, implausibility $I_h(a)$ is defined as:

$$I_h^2(a) = \frac{\left(L_h - f_h(a)\right)^2}{\mathrm{Var}_h(\mathrm{system})}. \tag{8}$$

Large values of $I_h(a)$ indicate that, taking into account all the uncertainties of the system (denominator of eq. 8), it is very unlikely to obtain acceptable matches between the model outputs and the observed data at input a. However, small values of $I_h(a)$ do not necessarily mean that the input value a is correct (Vernon *et al.* 2010). The Implausibility measure $I_h(a)$, as expressed in eq. (8), refers to multidimensional models (h number of output variables). A 1-D example of the above form, taking into account all the types of uncertainties present in our system (eq. 1) and based on the GP model as expressed in eq. (5), can be formulated as

$$I_i^2(a) = \frac{\left(L_i - E^*\left(T_i^{(r)}(a)\right)\right)^2}{\mathrm{Var}^*(T_i^{(r)}(a)) + \mathrm{Var}(\epsilon_i) + \mathrm{Var}(e_i)}, \quad (9)$$

where L_i our observed data, $E^*(T_i^{(r)}(a))$, $\mathrm{Var}^*(T_i^{(r)}(a))$ the posterior mean and posterior variance of Gaussian Process emulator and $\mathrm{Var}(\epsilon_i)$, $\mathrm{Var}(e_i)$ are the variances of the modelling and observation error, respectively. Index i, represent each velocity layer. The observed data L_i, for every discrete velocity layer associated with a hyperbolic event in a CMP gather, is the local maximum value of the semblance spectrum of that hyperbolic trend calculated from the observed offset X_j, amplitude values A_j and recorded time T_j. The non-implausible space is gradually reduced by applying multiple iterations of BHM. In order to identify the region of implausible input values, we use a cut - off limit based on Pukelsheim's 3σ rule (any continuous unimodal distribution at least 95 per cent of the probability is within three sigma of the mean) (Pukelsheim 1994). Based on that rule, input values a for which $I_h(a) > 3\sigma$ are considered implausible and are discarded. The iterative BHM procedure is usually repeated until the difference between the regions, after successive iterations, becomes small or the posterior variance is suitably small (Andrianakis *et al.* 2015).

As BRAINS model is multidimensional ($T_i^{(r)}$ is linked with ΔT_{0_i}, $\Delta V_{\mathrm{rms}_i}$, $V_{\mathrm{int.}_i}$ and ΔZ_i, referred as index h in eq. 8), we opt to build separate implausibilities for every output h. A simple combination between the implausibility measures can be performed by taking the maximum implausibility $I_M(a) = \max I_h(a)$ which can be used to find regions of input values a with large $I_M(a)$ values. Note that the application of BHM is a fast process as it excludes the implausible space without considering the full input and output space simultaneously, dissimilar to other calibration methods such as Markov Chain Monte Carlo (MCMC) or maximum likelihood methods where the calibration is performed taking into account all input / output parameters (Andrianakis *et al.* 2015).

A pictorial example of GP emulation with BHM calibration in seismic reflection data processing is presented in Fig. 3. The conventional semblance spectrum plots (Fig. 3a), for a number of CMP's along a profile, are picked to derive an initial estimate of T_0–V_{rms} pairs (red circles) associated with a number of seismic boundaries (Fig. 3b). The pairs do not include any sort of uncertainty measurement and are linearly interpolated between non–adjacent CMP positions (gray dashed lines). As a result, this process leads to unique T_0–V_{rms} and Z–$V_{\mathrm{int.}}$ volumes and unique subsurface images in time and depth domain. For the statistical approach, the T_0–V_{rms} pairs along with CMP gathers which contain the observed parameters $L = [A_j, X_j, T_j]$ transformed in the semblance space, are used as input data to the local (1-D) GP emulator to derive an estimate of the most probable functions evaluated at each picked pair. By means of calibration, we reduce the parameter space substituting the semblance spectrum by an implausibility spectrum which is calculated using eq. (8). In Fig. 3(c), a Z–$V_{\mathrm{int.}}$ map is presented, with the picked pairs being spatially linked with the pre-SDM image shown in Fig. 3(d). The coloured band inside the trend indicates different levels of implausibility. In the regions where the posterior mean is far from the observed values the implausibility is considered large (red colour), indicating that an input pair in that band is unlikely to give an output that will match the observations L. On the contrary, if we choose to make our pick in the lower implausibility regions (green areas), the posterior variance will decrease, with a simultaneous decrease of the non–implausible region. A further decrease of parameter space can be achieved by iteratively performing BHM in the non-implausible regions.

The process continues in all CMP locations where we provided prior pick information and terminates when one of the aforementioned criteria is reached. The posterior mean and variance estimations for the picked pairs, serve as a guide to perform uncertainty analysis along the profile using the multigather 2-D emulator aiming to produce probabilistic estimates in the intra-CMP gathers area.

Note that the implausibility map is not restricted to the Z–$V_{\mathrm{int.}}$ space but it is calculated for any combination of T_0 or Z with V_{rms} or $V_{\mathrm{int.}}$ pairs. Each implausibility pair has different shape and size, locally (in every CMP location) and also laterally (along CMP locations), incorporating the different level of uncertainty in each picked pairs and spatial positions. Also, the regions between the prior information picks in each map are bounded by the posterior $\pm\, 2\sigma$ curves (blue dashed curves), with the posterior mean function curve (solid black curve) intersecting regions of lowest implausibility. This interlayer representation of uncertainty can be achieved by interpolating the posterior results.

The final output of this process is a set of uncertainty quantification for all T_0, V_{rms}, V_{int} and Z parameters for each horizon of interest (Fig. 3d). An important by-product of the technique is that by quantifying the uncertainty of $V_{\mathrm{int.}}$ values, we can generate a set of velocity fields bounded by the $\pm 2\sigma$ curves and produce different realizations of pre-SDM images. The latter tool can be critical in regions with complex geology or for data rich in low frequency content and noise level, where a sole realization of imaged structures may not adequately identify risk at proposal drill sites.

3.3 Data pre-conditioning for input to BRAINS

As our primary goal is to develop a horizon based velocity model discretized in a number of layers (Appendix A1), the final version of the velocity field aims to produce flat CIG gathers and focused images in time and depth domain. Therefore, the processing steps are tailored appropriately to build an optimum velocity field which will be used as prior information to BRAINS algorithm. Concurrently, in order to clarify the target horizons of the profile we shaped the amplitude spectrum by eliminating the source bubble pulse coda and the source and receiver ghost notches in the shot domain.

The pre-stack de-signature and deghosting process combined with the reposition of the data through the application of pre-stack time migration (pre-STM)/pre-SDM, are the two key steps in the processing flow described below and they have a dual effect in improving BRAINS estimation. First, by improving the temporal resolution pre-stack, sharper reflections events become apparent in CMP domain, which are transformed into well-defined local maxima in the semblance space. As BRAINS and the process of BHM use the semblance spectrum (L observed data) as a tool to constrain the posterior results, the pre-stack deghosting gives extra precision to the model's outputs. Second, the pre-stack reposition of the data is mandatory, as it focuses the reflection events and eliminates the dip-dependence of stacking velocity ($V_{\mathrm{st.}}$), providing a better constrain to prior information (T_0, Z with V_{rms}, $V_{\mathrm{int.}}$ pairs).

3.3.1 *Time domain processing*

The raw shot gathers for line S310-07 are provided by Geoscience Australia (detailed acquisition parameters in Table 1, processing

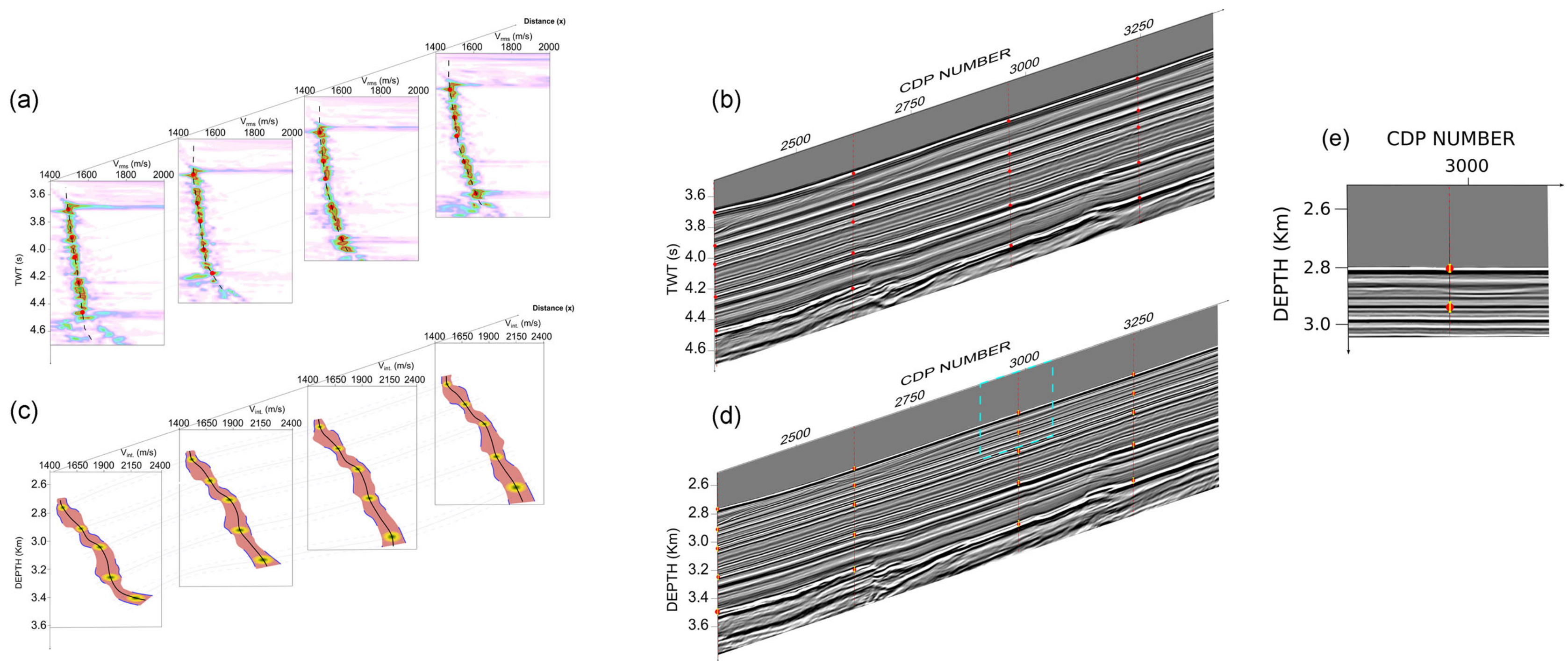

Figure 3. Schematic representation of the application of Gaussian Process and Bayesian History Matching (BHM) in seismic reflection data. (a) A number of semblance spectrum plots associated with CMP positions along a preSTM profile shown in (b). The T_0–V_{rms} pairs, at semblance maxima (red circles), can be picked to follow seismic boundaries. Between analysis locations, the T_0–V_{rms} pairs are linearly interpolated (dashed gray lines) but do not incorporate any uncertainty estimation. (c) Using GP and BHM, the semblance spectrum can be substituted by an implausibility map. Trends represent the implausibility map for Z–$V_{\mathrm{int.}}$ pairs, the latter being spatially linked with the pre-SDM figure shown in (d). Green regions, at prior picks, indicate low implausibility levels (most probable pairs) and red and yellow higher levels of implausibility. The user-defined picks, both in depth and velocity domain, are bounded by the $\pm 2\sigma$ posterior uncertainty curves (blue dashed curves) with the posterior mean function (black solid curves) passing through the regions of lowest implausibility. The probabilistic approach gives an uncertainty estimation for each layer along a profile in positions where we do not provide prior information to define a depth velocity volume (black solid curves along layers, posterior mean function–blue dashed curves along layers, posterior $\pm 2\sigma$). The yellow bars on the pre-SDM image (d) represent the depth uncertainty from our analysis. (e) Zoomed panel of the cyan dashed box in (d).

Table 1. Acquisition specifications for line S310-07.

Parameter	Value
Source type	Tuned point-source air-gun array
Gun type	Bolt 1500LL air guns
Nominal source volume	70.3 L (4290 cu in)
Nominal source pressure	13.7 Mpa (2000 psi)
Nominal source depth	7 $\pm$1 m
Shotpoint interval	37.5 m
Streamer type	Sercel Seal Solid
Number	1
Streamer Length	8100 m
Number of groups	648
Group length	12.5
Nominal streamer depth	10 $\pm$1 m
Nominal inline offset	94
Recording system	Sercel SEAL v5.2
Record length	12 s
Sample interval	2 ms
Low-cut filter/ slope	2 Hz at 6 dB/Oct, Digital Low-Cut: OFF
High-cut filter/ slope	200 Hz at 370 dB/Oct
Recording format	SEGD 8058 rev.1 32bbit IEEE

Table 2. Processing sequence applied to seismic line S310-07 (time domain).

S310-07
Reformat and geometry import – CDP spacing = 6.25 m – Nominal CDP fold = 108
Instrument delay correction = 100 ms, source–receiver datuming
Zero phase low cut Butterworth filter 4 Hz, 18 db/octave
Modelled debubble inverse filter (shot gathers)
Deterministic inverse filter for source's notch compensation (shot gathers) derived from post-stack amplitude spectrum
Receiver's notch compensation in $f-x$ domain (shot gathers)
CMP Sorting and Velocity analysis (every 312.5 m / 50 CMPs)
Straight ray isotropic Kirchhoff Pre Stack Time Migration (Pre-STM)
Spherical Divergence Correction
Outer Trace Mute and Stack
Time variant zero phase Butterworth filter:
10-20-100-125 at seabed (sb),
10-20-100-125 at sb + 0.3 s,
8-15-100,120 at sb + 0.6 s,
5-10-90-110 at sb + 0.9 s,
3-8-50-70 at sb + 2.5 s
Frequency – distance ($f-x$) deconvolution for random noise attenuation
Amplitude–phase Inverse Q compensation = 200
Cosmetic sea noise mute

sequence in Table 2). Initially, geometry acquisition information is imported to the profile and gun and receivers' static corrections are applied to the shot gathers to compensate for the tow depths of the source and streamer. A time-invariant low cut filter is used to reduce the low frequency swell noise. The first step for the spectrum shaping is to create a debubble operator to eliminate the source's bubble pulse coda. The inverse operator is modelled using the Nucleus source modelling package [Petroleum Geo services (PGS)] which takes into account the acquisition parameters, the volume and type of air guns and the physical parameters of the water (sound speed and temperature) during the seismic acquisition. The filter is convolved in the pre-stack (shot) domain as the periodicity of the bubble pulse is close to constant from shot to shot (Sargent *et al.* 2011). The source's notch effect was eliminated in the same domain, using a deterministic inverse filter constructed following the approach of Sargent *et al.* (2011). Although the deterministic inverse filters can be applied pre-stack, their periodicity and shape is tailored to the average observed notches observed in the stack amplitude spectrum. Similarly, the receiver's notch amplitude compensation is performed on a shot by shot basis by applying an automatic receiver's deghosting filter in the *f–x* domain, after plane wave decomposition and separation of up–going and down–going waves (Amundsen 1993).

The deep water environment of the segment (more than 2.5 Km depth from sea level) generates long path multiples that do not interfere with the signal of the sedimentary sequence. As a result, we chose not to apply any demultiple techniques. After sorting shot gathers into CMP gathers, several passes of manual velocity analysis and subsequent straight ray isotropic Kirchhoff pre-STM are performed, aiming at building a smooth velocity field appropriate to produce flat image gathers. The final velocity model is also used for divergence correction to compensate for geometrical spreading. Before stacking, the flat time gathers underwent an outer trace mute to avoid any stretch effects at far offsets.

In the post-stack domain, random noise elimination is achieved by application of frequency–distance (*f–x*) deconvolution (Canales 1984) and amplitude/phase inverse Q filter is applied to compensate for the attenuation during seismic wave propagation (Wang 2002). Time - variant bandpass filtering and cosmetic sea noise mute complete the processing of the profile in the time domain.

In Fig. 4, we present the comparison between images with (Figs 4a and b) and without (Figs 4c and d) notch compensation. The ghost free image shows optimum focusing and is characterized by a broadband amplitude spectrum (Fig. 4e). The retrieved frequency content improves the temporal resolution of the profile, which results to sharper seismic boundaries and by inference more constrain interpretation, especially at the shallow sedimentary sequence (arrows and curly brackets in Figs 4b and d). Note, however, that the presence of basalts at around 4.5 s TWT (Maloney *et al.* 2011) attenuates the high frequency content of the seismic energy (Maresh *et al.* 2006) resulting in a poor reflectivity in the sub-basalt region.

3.3.2 Depth domain processing

Although the processing flow in the time domain yielded acceptably focused images, the 1-D representation of the velocity model used in the time migration algorithm (Hubral 1977; Black & Brzostowski 1994) sets a limit to the precision of the velocity model building (Jones 2010, 2012). Thus, we opted to use the final version of the pre-STM velocity field as a starting model to perform isotropic Kirchhoff pre-SDM on the deghosted CMP gathers. As our well positions lie in an area with a relatively simple geological structure (Fig. 2b), we chose to run subsequent passes of vertical update (Deregowski 1990) to refine our input velocity field until acceptably flat CIG gathers were produced. The resulted depth migrated images gathers are stretched back to time using the smoothed version of the final velocity field for filtering and cosmetic final residual moveout correction (RMO) and converted back to depth domain for stacking. This additional editing of velocity field assisted to constrain better the prior information for input to the Bayesian model and simultaneously assured that the velocity model is suitable to pre-SDM applications.

Even in an environment with subhorizontal layers and relatively simple subsurface structure like our area of interest, the pre-STM and pre-SDM profiles show some structural differences, with the latter showing local sharpening of the faulted zones close to well locations (Figs 5a and b). Furthermore, the amplitude

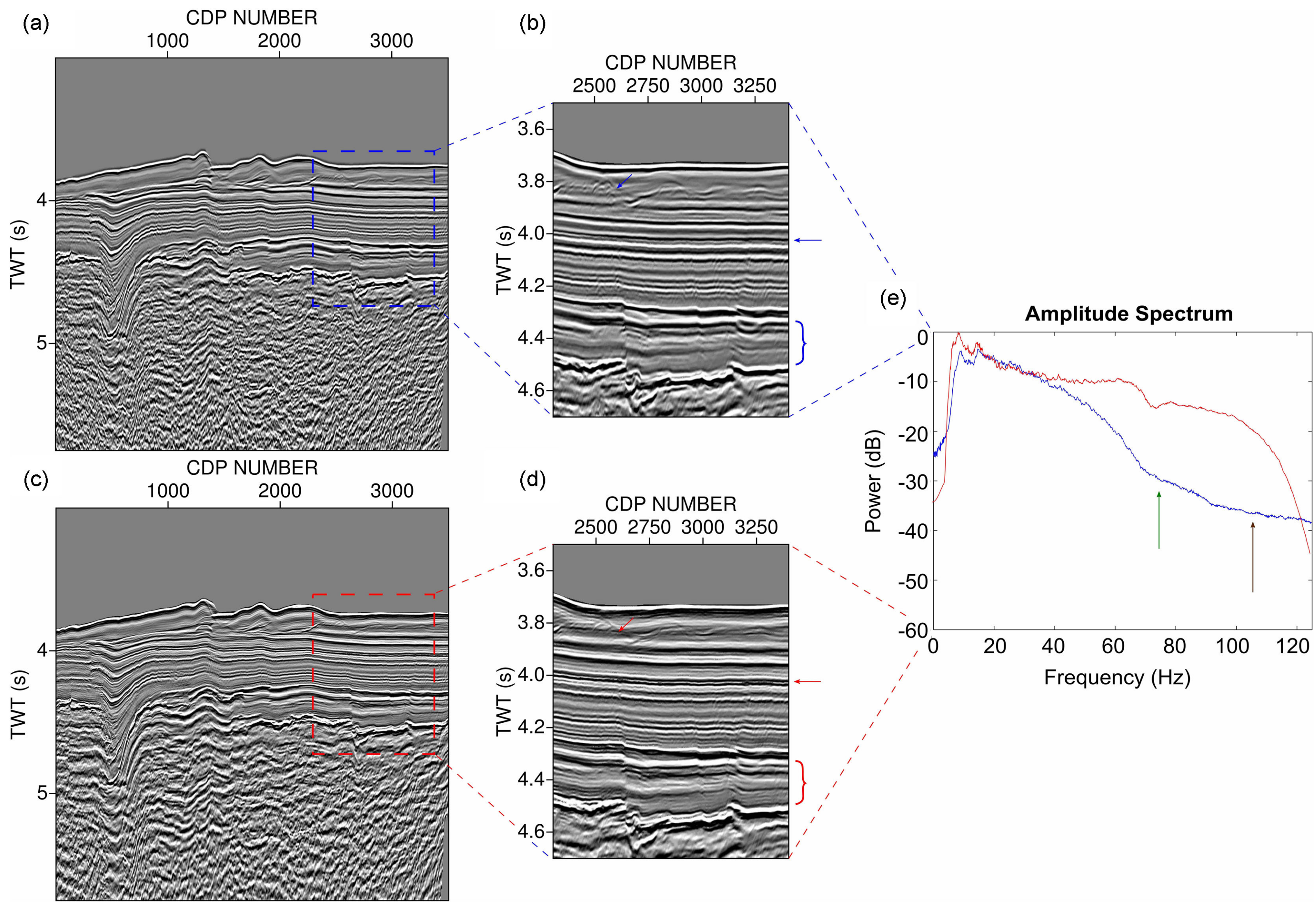

Figure 4. Comparison between pre-STM images with and without notch compensation. (a and b) Pre-STM profile and zoomed panel close to well locations produced following the processing root of Table 2 without any notch elimination. (c and d) Same as in (a) and (b) but with source's and receiver's notches elimination performed pre-stack. Note the improved temporal resolution in all the profile, with the most prominent differences between (a) and (c) indicated in blue and red arrows, respectively. (e) Amplitude spectra of the images (blue from panel (b), red from panel (d)) showing the retrieved amplitude after compensating for source and receiver notches (green and brown arrows).

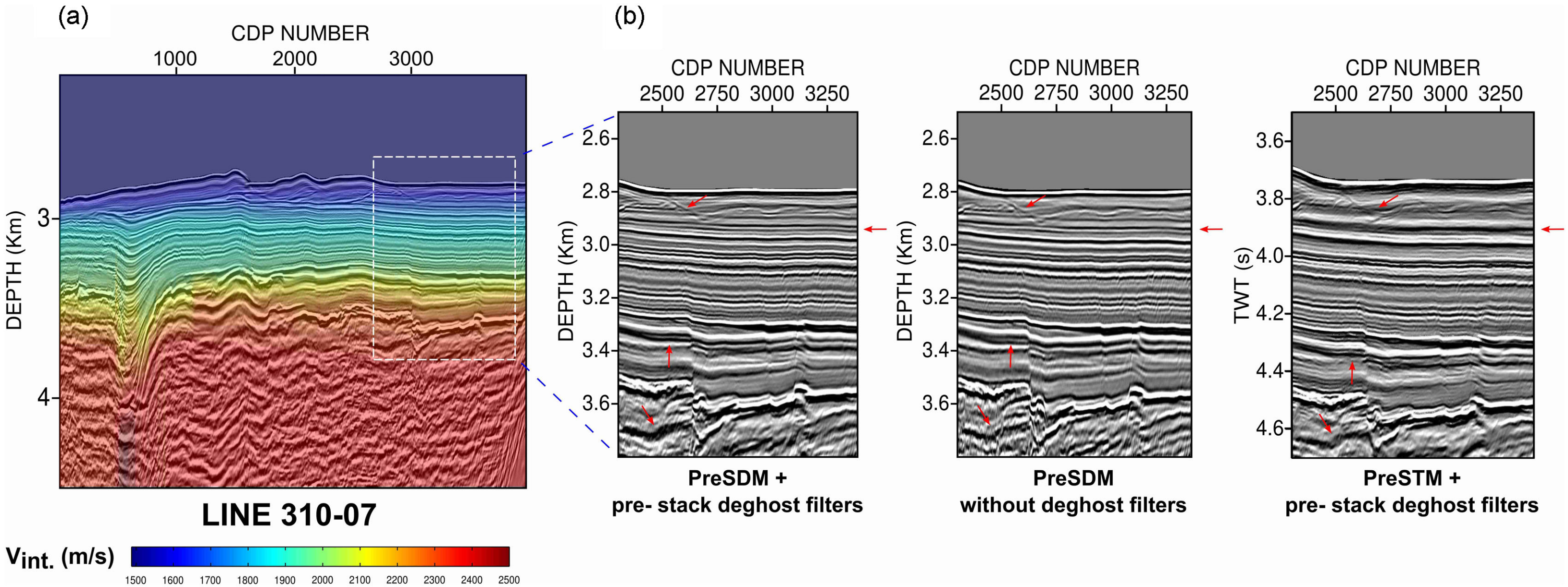

Figure 5. (a) Pre-SDM image generated using the final version (prior) $V_{\mathrm{int.}}$ velocity field as input to migration algorithm (superimposed). (b) Pre-SDM/pre-STM images with and without pre-stack amplitude shaping. Red arrows indicate the most pronounced structural and spatial/temporal differences, in the shallowest and deeper parts of the images, emerged after application of depth migration and inverse filtering in the pre-stack domain. Although the geological structure is relatively simple, the image differences are locally considerable indicating the need for optimum elimination of ghost notches and velocity refinement through an iterative pre-SDM loop to better constraint the prior velocity information.

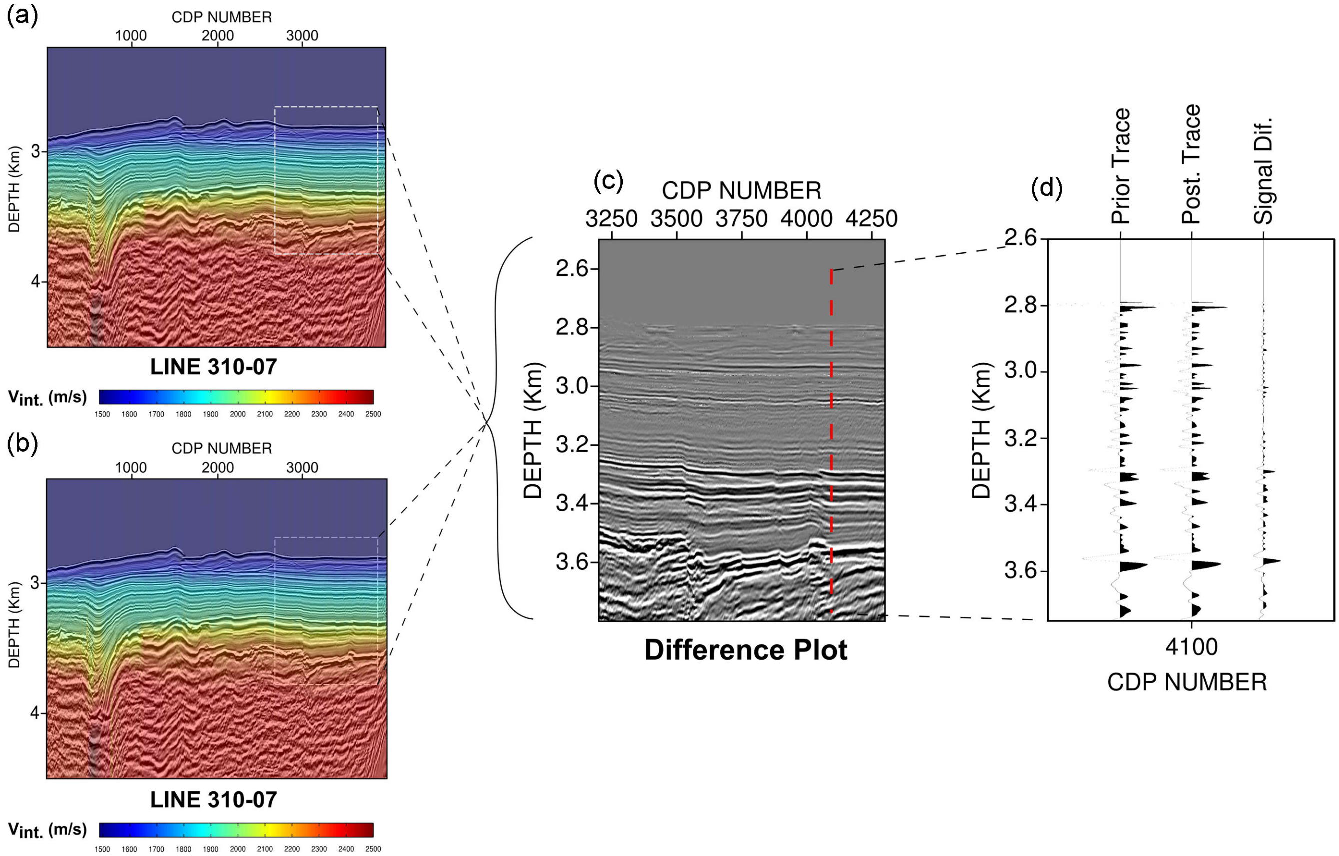

Figure 6. Comparison between prior and posterior mean pre-SDM images. (a) Image generated using the prior V_{int} velocity field (superimposed). (b) Image using the posterior mean V_{int} velocity field (superimposed). (c) The velocity fields and images do not present any significant differences, therefore possible structural changes can become apparent after using a structural difference plot, which is the result of subtracting the posterior mean image (b) from prior image (a). The image features' changes are more pronounced in the deeper parts of the profile as a direct consequence of top–down reposition of the signal. (d) Example of signal difference extracted from a depth window of CDP number 4100 (red dashed line in panel (c)), as calculated by subtracting the posterior from the prior signal.

compensation in the seismic gathers in time domain has generated a profile in depth domain with optimum spatial resolution and focusing (Figs 5a and b). Thus, the application of pre-stack inverse filters serves as an amplitude shaping tool in both domains, in contrast with implementing deterministic post-stack inverse filters (Sargent *et al.* 2011), which can produce flat amplitude spectrum and improved image resolution only in the time domain.

4 RESULTS AND DISCUSSION

Using the final version of the $t_0 - V_{\mathrm{rms}}$, $t_0 - V_{\mathrm{int.}}$ pairs as prior information for BRAINS along with the deghosted preSTM image gathers and performing BHM to reduce the parameter space, we calculate the posterior distribution of t_0, V_{rms}, V_{int} and z for each CMP value and make uncertainty estimations for the variables of interest. Initially, the posterior mean $V_{\mathrm{int.}}$ field was used as input to the depth migration algorithm. A comparison between the images produced using the prior and posterior mean V_{int} fields is given in fig 6. The pre-SDM profiles do not indicate any major structural differences as the models used are nearly identical. This is a direct consequence of the Gaussian Process model used and the prior picks made, as the mean function in eq. (5) encodes the hyperbolic approximation of the seismic wave propagation. As the latter is also used to define the moveout trajectory for semblance spectrum calculation associated with hyperbolic events in CMP positions along a profile, the closest the prior t_0–V_{rms} or t_0–$V_{\mathrm{int.}}$ picks are to the local maxima semblance value, the less difference will be observed between prior and posterior mean models and by inference depth images.

Differences are resolved after subtracting the posterior mean pre-SDM image (Fig. 6b) from its prior equivalent (Fig. 6a), resulting in a structural difference plot (Figs 6c and d). The images' dissimilar features are now emphasized, indicating regions of differential depth shift. As the migration algorithm repositions the time signal to the depth domain in a top-down basis, the cumulative differences of velocity field with respect to depth get larger and map to more pronounced depth image shifts. Note that as the velocity fields show minor differences, this effect generates only a vertical structural stretch with no resolvable lateral structural changes.

In terms of depth predictions, although we used an isotropic approximation of pre-SDM, the tie with the borehole information is acceptable with a misfit of approximately 4 per cent (21 m) at the glauconitic sandstones level (Figs 7a and b). The large misfit at the bottom shales level is attributed to the indistinct reflectivity boundary between limestones and shales (Figs 7a and b). Note, however, that the observed depths from DSDP-258 are consistent with the $\pm\, 2\sigma$ credibility intervals. This result reassures us that

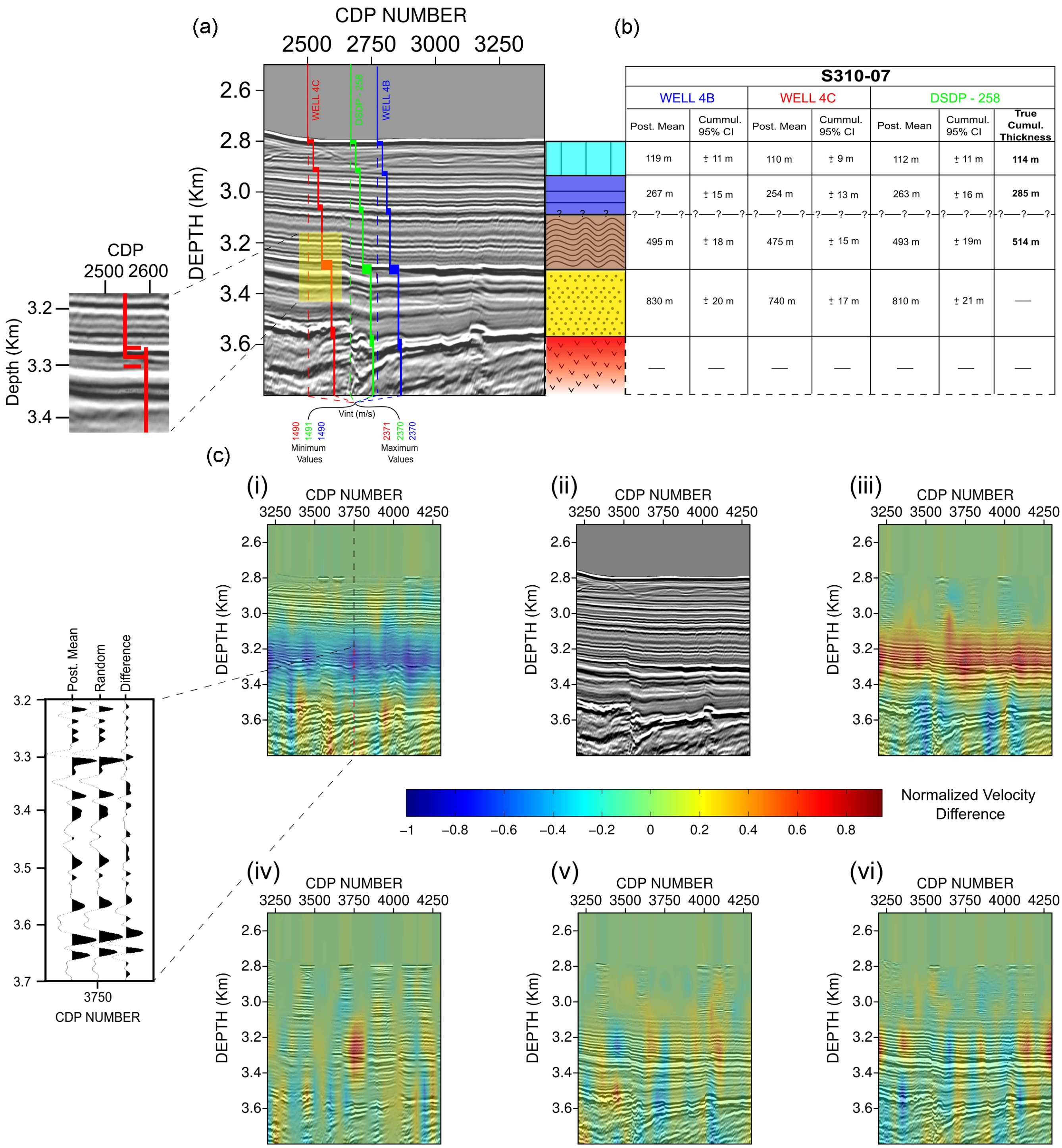

Figure 7. Posterior depth results and probabilistic imaging. (a) Pre-SDM image for S310-07 profile. Dashed vertical lines represent the wells' locations, with the posterior range of interval velocity/depth values for each layer superimposed as filled coloured regions (red, green and blue colours for Well 4C, DSDP-258 (Well 4A) and Well 4B, respectively). Zoomed panel shows the region associated with the yellow rectangle as an example of the posterior mean and $\pm 2\sigma$ trends for top glauconitic sandstones (red solid trend in zoom represent posterior mean values, dashed lines in zoom the $\pm 2\sigma$ intervals respectively). (b) The predictions for the cumulative thickness of drilling targets for each well location, associated with the lithological interpretation from Fig. 2. (c) A number of pre-SDM structural difference plots, using $V_{\mathrm{int.}}$ sampled from the posterior distribution. The superimposed coloured map represents the normalized difference between the randomly generated $V_{\mathrm{int.}}$ velocity fields used to produce each profile and the posterior mean. Panels c(i) and c(iii) demonstrate the $\pm 2\sigma$ end members for black shales velocity layer with the remaining layers preset to take random values from the posterior distribution. Zoomed panel from c(i) shows how the difference plot is generated. Fig. c(ii) same as in (a). Panels c(iv), c(v) and c(vi) represent fields allowed to span the total $V_{\mathrm{int.}}$ space of the posterior distribution.

our posterior mean velocity field is a good representation of the local velocity field and, by inference, can be used to make predictions about the depths to horizons in the new well locations (Figs 7a and b).

The uncertainty quantification not only results in a numerical estimation of depth values for key horizons, but can be also used to generate a set of probabilistic images by sampling $V_{\mathrm{int.}}$ values from the posterior distribution and using the latter as input to pre-SDM algorithm. In Fig. 7(c), we present a number of structural difference plots, produced by subtracting each resulted pre-SDM image realization, derived using a probabilistic velocity field, from the posterior mean image. The plots display a number of probable depth and shape positions for geological boundaries of interest, in accordance with the differences between the sampled velocity fields and the posterior mean velocity field [Figs 7c(i) and (iii) $\pm 2\sigma$ end members for posterior black shales velocity, Figs 7c(iv)–(vi) randomly generated values for all velocity layers, Fig. 7c(ii) posterior mean image). In positions where the differences are closer to extreme values, the local image features start changing in shape (localized red maxima in Figs 7c(iii) and (iv)).

The randomly generated values, bounded by the $\pm\ 2\sigma$ credibility intervals for every CMP position and every velocity layer, incorporate a confidence measure associated to each picked pair which is a combination of the observed data (amplitude values A_{ij}, recorded traveltime $T_{ij}^{(r)}$, distance X_j), and prior picks positions. Thus, the retrieved vertical pattern of blue (negative) and red (positive) regions in the normalized velocity difference plots of Fig. 7(c) approximates the Gaussian Process pattern depicted in Fig. 3(c), where the $\pm\ 2\sigma$ curves, along a velocity layer, show decreased uncertainty close to the prior picked CMP positions and increased between them. These regions have a spacing of approximately 50 CMPs positions, driven by the velocity picking spacing used to generate the prior velocity model for time and depth migration (Table 2). We expect that the mapping of the uncertain nature of velocity models to image realizations, especially in areas with complex geological structures such as salt diapirs or basalt intrusions, is critical to constrain better the most probable interpretations and risk.

The observed misfit between the modelled mean and true depths at the glauconitic sandstones level can be primarily attributed to the isotropic approximation of BRAINS and the migration algorithm used. As described in expressions (5)–(7), the Gaussian process emulator does not include an explicit representation of epsilon (ϵ) and delta (δ) anisotropic parameters (Thomsen 1986), therefore these terms are not statistically quantified as an output from the model. The uncertainty related with anisotropic conditions is integrated in our system into the model discrepancy term which value is set accordingly to accommodate the mismatch in the predicted depths and observed data, driven primarily by excluding Thomsen's ϵ and δ parameters. This approach was chosen in order to avoid narrow posterior variances which would indicate overconfident depths predictions for the drilling targets, predictions that could not be supported for the result extracted using an isotropic depth migration algorithm alone, without the confirmation from independent observations (well logs).

Although indirect, this compensation of the anisotropic parameters through a unified discrepancy term can be considered as the optimum solution in our system. Firstly, the lack of any wireline log information concerning seismic velocities does not facilitate the process of anisotropic velocity model building as the true velocity values could be implemented to better constrain the prior information in our model and simultaneously be used as a starting point for higher order NMO correction (fourth-order correction, η parameter). Furthermore, due to the uncertain tie between the observed reflectivity in the final pre-STM/pre-SDM images and the lithological boundaries (especially at the boundary between limestones to black shales), any scaling of the target horizons to match the observed depths (Davies *et al.* 1974) using an inferred δ parameter value is impractical and contains the risk of assigning observed reflectivities to incorrect geological boundaries and hence depths. As a result, trying to infer the anisotropic parameters and provide their uncertainty estimations, without any well control, was a task prone to uncertainties that could compromise the predictions of velocities and depths for the horizons of interest.

However, there is an additional, more subtle reason that justifies our approach. It has been shown (Al-Chalabi 2014), that the inclusion of a fourth-order term during NMO correction (estimation of η parameter) is associated with a large increase in the observed variance compared to the simpler second-order hyperbolic approximation mainly due to the strong anti-correlated nature between V_{nmo} and η variables. This result indicates, that an anisotropic approach during the velocity analysis stage combined with anisotropic migration algorithms, although may result to better focusing of the final image and possibly better prior/posterior mean depth results, does not lead to a better uncertainty quantification of velocity values.

5 CONCLUSION

We have presented a method to quantify the uncertainty of depths and related values in seismic reflection data processing. Our seismic reflection processing strategy was separated into two distinct parts. First, we aimed to improve the temporal and spatial resolution of the region close to the planned well locations by performing source's and receiver's notch compensation in the pre-stack domain. Then, we focused on the velocity model building in the time and depth domain in order to generate well focused images and constraint prior information for input to the BRAINS model. By using Gaussian Process emulators conjointly with iterative BHM, we managed to retrieve the depths of the key horizons as known from DSDP-258 borehole and make predictions about the expected depths of same horizons for wells 4B and 4C, respectively.

As the probabilistic approach results in a distribution estimation for V_{int}, we generated sets of new velocity models and perform pre-SDM to produce different image realizations. In this way, we were able to map differences in velocity models to differences in image features for our horizons of interest.

The GP emulators are deliberately parametrized to exclude explicit uncertainty estimations for anisotropic parameters (ϵ, δ). Instead, the anisotropic effects during seismic wave propagation are unified in the model discrepancy term (ϵ_{ij} or σ_{n_i}), a term which is easier to tune and with the synergy of prior information of picked $\{V_{\mathrm{rms}}, t_0\}$ or $\{V_{\mathrm{int.}}, t_0\}$ pairs, it allows constrained posterior results. The inclusion of the anisotropic terms as independent variables in our model along with their explicit uncertainty estimation, would require well log information concerning true seismic velocities and also well to seismic tie to unambiguously map observed reflectivities from seismic data to lithological boundaries. Even in that case, their incorporation could pose problems concerning the robustness of their uncertainty estimations, as in time domain the terms are accessed solely through η parameter (Alkhalifah & Tsvankin 1995; Alkhalifah 1997), a term that is strongly coupled to the small-offset moveout velocity (V_{nmo}), that a useful uncertainty estimation is in question.

The statistical model described in this paper is based on the discrete layer velocity model representation and can be easily coupled with a layer-based tomographic inversion scheme. The challenge will be to incorporate an analogous model to gridded or hybrid velocity model representations (Jones *et al.* 2007) for complex geological structures, where the velocity regime is controlled by a combination of vertical compaction gradients and sharp velocity contrasts.

ACKNOWLEDGEMENTS

The seismic reflection profile S310-07 was provided by Geoscience Australia. GNS Globe Claritas software was used for seismic reflection processing; PGS Nucleus modelling package was used to compute theoretical source signature and Matlab Mathworks for statistical analysis; Seismic Un*x (Cohen & Stockwell, 2010) was used to plot sections for publication.

REFERENCES

Abrahamsen, P., Omre, H. & Lia, O., 1991. Stochastic models for seismic depth conversion of geological horizons, *SPE,* **23 138,** 329–341.

Al-Chalabi, M., 1994. Seismic velocities—A critique, *First Break,* **12,** 589–596.

Al-Chalabi, M., 2014. *Principles of Seismic Velocities and Time-to-Depth Conversion,* EAGE Publications.

Alkhalifah, T., 1997. Velocity analysis using nonhyperbolic moveout in transversely isotropic media, *Geophysics,* **62,** 1839–1854.

Alkhalifah, T. & Tsvankin, I., 1995. Velocity analysis for transversely isotropic media, *Geophysics,* **60,** 1550–1566.

Amundsen, L., 1993. Wavenumber–based filtering of marine point–source data, *Geophysics,* **58,** 1335–1348.

Andrianakis, I., Vernon, I.R., McCreesh, N., McKinley, J.T., Oakley, J.E., Nsubuga, R.N., Goldstein, M. & White, R.G., 2015. Bayesian history matching of complex infectious disease models using emulation: a tutorial and a case study on HIV in Uganda, *PLOS Comput. Biol.,* **11,** e1003968.

Bickel, S.H., 1990. Velocity–depth ambiguity of reflection traveltimes, *Geophysics,* **55,** 266–276.

Black, J.L. & Brzostowski, M.A., 1994. Systematics of time–migration errors, *Geophysics,* **59,** 1419–1434.

Borissova, I., 2002. *Geological framework of the Naturaliste Plateau,* Geoscience Australia Record 2002/20, 2002.

Bradshaw, B.E., Rollet, N., Totterdell, J.M. & Borissova, I., 2003. *A revised structural framework for frontier basins on the southern and southwestern Australian continental margin,* Geoscience Australia Record, 2003/03.

Caiado, C.C.S. & Goldstein, M., 2015. Bayesian uncertainty analysis for complex physical systems modelled by computer simulators with applications to tipping points, *Commun. Nonlinear Sci. Numer. Simul.,* **26,** 123–126.

Caiado, C.C.S., Hobbs, R.W. & Goldstein, M., 2012. Bayesian strategies to assess uncertainty in velocity models, *Bayesian Anal.,* **7,** 211–234.

Canales, L., 1984. *Random noise reduction: SEG Technical Program, Expanded Abstracts*, pp. 525–527. doi:10.1190/1.1894168.

Chen, J. & Schuster, G.T., 1999. Resolution limits of migrated images, *Geophysics,* **64,** 1046–1053.

Chitu, D.A., Al-Ali, M.N. & Verschuur, D.J. (2008). *Assessing estimated velocity-depth models: finding error bars in tomographic inversion, Geophysics,* **73,** VE223–VE233.

Cohen, J.K. & Stockwell, J.W., Jr, 2010. *CWP/SU: Seismic Un*x Release No. 42: an open source software package for seismic research and processing, Center for Wave Phenomena*, Colorado School of Mines.

Craig, P.S., Goldstein, M., Seheult, A.H. & Smith, J.A., 1997. Pressure matching for hydrocarbon reservoirs: a case study in the use of Bayes linear strategies for large computer experiments (with discussion), in *Case Studies in Bayesian Statistics III,* pp. 37–93. eds Gatsonis, C., Hodges, J.S., Kass, R.E., McCulloch, R.E., Rossi, P. & Singpurwalla, N.D., Springer-Verlag.

Cumming, J.A. & Goldstein, M., 2009. Bayes linear uncertainty analysis for oil reservoirs based on multiscale computer experiments, in *The Oxford Handbook of Applied Bayesian Analysis,* pp. 241–270, eds O'Hagan, A. & West, M., Oxford University Press.

Davies, T.A. *et al.*, eds, 1974. Shipboard site reports, site 258, in *Initial Reports of the Deep Sea Drilling Project*, Vol. 26, pp. 359–414, U.S. Government Printing Office.

Deregowski, S.M., 1990. Common-offset migrations and velocity analysis, *First Break,* **8,** 225–234.

Direen, N.G., Borissova, I., Stagg, H.M.J., Colwell, J.B. & Symonds, P.A., 2007. Nature of the continent-ocean transition zone along the southern Australian continental margin: a comparison of the Naturaliste Plateau, SW Australia, and the central Great Australian Bight sectors, in *Imaging, Mapping and Modelling continental lithosphere extension and breakup,* Vol. 282, pp. 235–261, eds Karner, G.D., Manatschal, G. & Pinheiro, L.M., Geological Society (London) Special Publication.

Dix, C.H., 1955. Seismic Velocities from Surface Measurements, *Geophysics,* **20,** 68–86.

Hawkins, K., Leggott, R., Williams, G. & Kat, H., 2001. Addressing anisotropy in 3-D prestack depth migration: a case study from the Southern North Sea, *Leading Edge,* **20,** 528–543.

Hobbs, R.W., Huber, B. & Bogus, K., 2017. *Tectonic, paleoclimate, and paleoceanographic history of the Mentelle Basin and Naturaliste Plateau at southern high latitudes during the Cretaceous*, doi:10.14379/iodp.sp.369.2016.

Hubral, P., 1977. Time migration—some ray theoretical aspects, *Geophys. Prospect.,* **25,** 738–745.

Jones, I.F., 2010. *An Introduction to: Velocity Model Building,* EAGE Publications, p. 295.

Jones, I.F., 2012. Tutorial: Incorporating near-surface velocity anomalies in pre-stack depth migration models, *First Break,* **30,** 47–58.

Jones, I.F., 2014. Estimating subsurface parameter fields for seismic migration: velocity model building, *Encyclopedia of Exploration Geophysics,* U1-1–U1-24.

Jones, I.F., Surgue, M.J. & Hardy, P.B., 2007. Hybrid gridded tomography, *First Break,* **25**(4), 35–41.

Journel, A.G. & Huijbregts, C.H., 1978. *Mining Geostatistics*, Academic Press, p. 600.

Ko, J. & Fox, D., 2009. GP-BayesFilters: Bayesian filtering using Gaussian process prediction and observation models, *Autonomous Robots,* **27,** 75–90.

Kosloff, D.D. & Sudman, Y., 2002. Uncertainty in determining interval velocities from surface reflection seismic data, *Geophysics,* **67,** 952–963.

Kuypers, M.M.M., Pancost, R.D. & Damste, J.S.S., 1999. A large and abrupt fall in atmospheric CO_2 concentration during Cretaceous times, *Nature,* **399,** 342–345.

Landa, E., 1991. Interpretation of velocity estimates from coherency inversion, *Geophysics,* **56,** 1377–1383.

Lewis, L., Caers, J. & Sava, P., 2015. Assessing seismic uncertainty via geostatistical velocity-model perturbation and image registration: An application to subsalt imaging, *Leading Edge,* **34,** 1064–1066, 1068–1070. doi:10.1190/tle34091064.1.

Lines, L., 1993. Ambiguity in analysis of velocity and depth, *Geophysics,* **58,** 596–597.

Maloney, D., Sargent, C., Direen, N.G., Hobbs, R.W. & Grocke, D.R., 2011. Re-evaluation of the Mentelle Basin, a polyphase rifted margin basin, offshore southwest Australia: new insights from integrated regional seismic datasets, *Solid Earth,* **2,** 107–123.

Maresh, J., White, R.S., Hobbs, R.W. & Smallwood, J.R., 2006. Seismic attenuation of Atlantic margin basalts: observations and modeling, *Geophysics,* **71,** B211–B221.

Matheron, G., 1973. The Intrinsic Random Functions and Their Applications, *Advances in Applied Probability,* **5,** 439-468.

Messud, J., Reinier, M., Prigent, H., Guillaume, P., Coléou, T. & Masclet, S., 2017. Extracting seismic uncertainties from tomographic velocity inversion and their use in reservoir risk analysis, *Leading Edge,* **36,** 127–132.

Neidell, N.S. & Taner, M.T., 1971. Semblance and other coherency measures for multichannel data, *Geophysics,* **63,** 482–497.

O'Hagan, A., 2006. Bayesian analysis of computer code outputs: a tutorial, *Reliability Engineering and System Safety,* **91,** 1290–1300.

Powell, C.M., Roots, S.R. & Veevers, J.J., 1988. Pre-breakup continental extension in East Gondwanaland and the early opening of the eastern Indian Ocean, *Tectonophysics,* **155,** 261–283.

Pukelsheim, F., 1994. The three sigma rule, *Am. Stat.,* **48,** 88–91.

Rasmussen, C.E. & Williams, C.K.I., 2006. *Gaussian Processes for Machine Learning,* MIT Press, p. 245.

Ripley, B.D., 1991. *Statistical Inference for Spatial Processes,* Cambridge Univ. Press, p. 148.

Royer, J.Y. & Coffin, M.F., 1992. Jurassic to Eocene plate tectonic reconstructions in the Kerguelen Plateau region, in *Proceedings of the Ocean Drilling Program, Scientific Results,* Vol. 120, pp. 917–928, eds Wise, S.W., Jr & Schlich, R.

Sargent, C., Hobbs, R.W. & Grocke, D.R., 2011. Improving the interpretability of air-gun seismic reflection data using deterministic filters: a case history from offshore Cape Leeuwin, southwest Australia, *Geophysics,* **76,** B113–B125.

Thomsen, L., 1986. Weak elastic anisotropy, *Geophysics,* **51,** 1954–1699.

Tieman, H.J., 1994. Investigating the velocity–depth ambiguity of reflection traveltimes, *Geophysics,* **59,** 1763–1773.

Vernon, I., Goldstein, M. & Bower, R.G., 2010. Galaxy formation: a Bayesian uncertainty analysis, *Bayesian Anal.,* **5,** 619–670.

Wang, Y., 2002. A stable and efficient approach of inverse Q filtering, *Geophysics,* **67,** 657–663.

APPENDIX: BAYESIAN MODELS AND GAUSSIAN PROCESS IN SEISMIC REFLECTION

In the following, we will briefly describe the 1-D and 2-D Gaussian Process emulators used. See (Caiado *et al.* 2012) for a full description of the models.

A1 1-D emulator

Suppose a discretized subsurface model, with a finite number of interfaces b_i and a given array of source–receiver pairs, S_j and R_j, containing m pairs. All the pairs are symmetrically placed around a CMP, with X_j being the distance between S_j and R_j. As the medium is discretized, we can associate to every layer i, a two way traveltime T_{0_i} with its time increment ΔT_{0_i}, a root-mean-square velocity V_{rms_i} with its increment $\Delta V_{\mathrm{rms}_i}$ and a thickness ΔZ_i. Furthermore, let T_{ij} be the real time for a wave ray to propagate from seismic source S_j to detector R_j, by refracting at interfaces b_i to b_{i-1}, reflecting at b_i and refracting back to the receiver's position. In case of parallel boundaries and isotropic conditions, the real traveltime T_{ij} is defined as

$$T_{ij} = \sqrt{T_{0_i}^2 + \left(\frac{X_j}{V_{\mathrm{rms}_i}}\right)^2} + \epsilon_{ij}, \tag{A1}$$

where ϵ_{ij} counts for the modelling error due to propagating approximations and isotropic assumptions.

Now, the recorded traveltime $T^{(r)}$ is a combination of the real traveltime T_{ij} plus a set of recording errors e_{ij}, resulting in the equation

$$T_{ij}^{(r)} = \sqrt{T_{0_i}^2 + \left(\frac{X_j}{V_{\mathrm{rms}_i}}\right)^2} + \epsilon_{ij} + e_{ij}. \tag{A2}$$

A generalization of eqs (A1) and (A2) uses Gaussian Process techniques, works in function space instead of weight space and compensates for the lack of flexibility of the standard regression methods (Rasmussen & Williams 2006).

For 1-D case, we assume that a set of traveltimes, related to a certain interface in a CMP gather, is a sample of a continuous function with a hyperbolic trend. If a finite set of times in that curve follows a multivariate Gaussian distribution, we can think that every reflection hyperbola in a CMP gather is a Gaussian Process (GP) over offset x.

In a function form, the recorded traveltime curve, for a particular layer, $\mathcal{T}_i^{(r)}$ is a Gaussian Process

$$\mathcal{T}_i^{(r)}(x)|\Delta T_{0_{(1,\ldots i)}}, \Delta V_{\mathrm{rms}_{(1,\ldots,i)}} \sim \mathcal{GP}(m_{t_i}(x), k_i(x, x')) \tag{A3}$$

with mean and square exponential covariance functions

$$\begin{aligned} m_{t_i}(x) &= (t_{0_i}^2 + x^2 \upsilon_{\mathrm{rms}_i}^{-2})^{1/2} \\ k_i(x, x') &= \sigma_{n_i} + \sigma_{s_i} exp\left(-\tfrac{(x-x')^2}{d_i}\right) \end{aligned} \tag{A4}$$

where x and x' define two random points from the offset space in a single CMP, σ_{s_i} is a scale parameter, σ_{n_i} is a noise parameter and d_i is a length parameter. The last parameters are regarded as constants or can be set manually. The joint prior for both $\Delta T_{0_{(1,\ldots i)}}$ and $\Delta V_{\mathrm{rms}_{(1,\ldots,i)}}$ is given by

$$\begin{pmatrix} \Delta T_{0_{(1,\ldots i)}} \\ \Delta V_{\mathrm{rms}_{(1,\ldots,i)}} \end{pmatrix} \sim \mathcal{N}\left(\begin{pmatrix} \mu_{t_{0_i}} \\ \mu_{\upsilon_{(i)}} \end{pmatrix}, \Sigma_{(t_0, \upsilon_{\mathrm{rms}_i})}\right) \tag{A5}$$

and their prior distribution is written as

$$\pi(\upsilon_{\mathrm{rms}}, t_0) = \prod_{i=1}^{n} \pi(\Delta t_{0_i}, \Delta_{\upsilon_{\mathrm{rms}_i}}) \tag{A6}$$

with $\pi(\Delta t_{0_i}, \Delta_{\upsilon_{\mathrm{rms}_i}})$, the density of the joint prior in (A5).

In a similar manner, we can express the likelihood function of the GP in (A3) as

$$\pi(t_i^{(r)}(x)|\upsilon_{\mathrm{rms}_i}, t_{0_i}) = \pi\left(t_i^{(r)}(x)|\Delta t_{0_{(1,\ldots,i)}}, \Delta \upsilon_{\mathrm{rms}_{(1,\ldots,i)}}\right). \tag{A7}$$

Finally, the posterior distribution is given as the combination of the prior distribution (A6) and the likelihood (A7), resulting in the following expression

$$\pi(\upsilon_{\mathrm{rms}}, t_0|t^{(r)}) = \pi(\upsilon_{\mathrm{rms}}, t_0) \int_x \frac{\pi\left(t_i^{(r)}(x)|\Delta t_{0_{(1,\ldots,i)}}, \Delta \upsilon_{\mathrm{rms}_{(1,\ldots,i)}}\right)}{\pi(t^{(r)}(x))} \mathrm{d}x \tag{A8}$$

with $\pi(t^{(r)}(x))$, a normalizing constant that can be evaluated numerically.

A2 2-D emulator

For the 2-D case, we expand the 1-D Gaussian Process into a multi-gather representation by assuming that the variables ΔT_{0_i}, $\Delta V_{\mathrm{rms}_i}$, V_{int_i} and ΔZ_i, for every geophysical boundary, follow a GP over the CMP positions (x_c) along a profile. As a result, for the recorded traveltime $\mathcal{T}_i^{(r)}$ we have

$$\begin{aligned} &\mathcal{T}_i^{(r)}(x, x_c)|\Delta T_{0_{(1,\ldots i)}}(x_c), \Delta V_{\mathrm{rms}_{(1,\ldots,i)}}(x_c) \\ &\sim \mathcal{GP}\left(m_{t_i}(x, x_c), k_i(x, x', x_c)\right) \end{aligned} \tag{A9}$$

with mean and square exponential covariance functions

$$\begin{aligned} m_{t_i}(x, x_c) &= \left(t_{0_i}(x_c)^2 + x^2 \upsilon_{\mathrm{rms}_i}(x_c)^{-2}\right)^{1/2} \\ k_i(x, x', x_c) &= \sigma_{n_i}(x_c) + \sigma_{s_i}(x_c)\exp\left(-\tfrac{(x-x')^2}{d_i(x_c)}\right). \end{aligned} \tag{A10}$$

In a similar manner, as $\Delta V_{\mathrm{rms}_i}$ and ΔT_{0_i} follow a GP, they take the following form

$$\Delta V_{\mathrm{rms}_i}(x_c) \sim \mathcal{GP}\left(m_\upsilon(x_c), \sigma_{n\upsilon_i} + \sigma_{s\upsilon_i} \exp\left(\frac{(x_c - x_c')^2}{d_{\upsilon_i}}\right)\right) \quad \text{(A11)}$$

$$\Delta T_{0_i}(x_c) \sim \mathcal{GP}\left(m_{t_0}(x_c), \sigma_{nt_i} + \sigma_{st_i} \exp\left(\frac{(x_c - x_c')^2}{d_{t_i}}\right)\right) \quad \text{(A12)}$$

with $m_\upsilon(x_c)$, $m_{t_0}(x_c)$ polynomial functions, x_c, x_c' two different CMP locations along the profile and $\sigma_{n\upsilon_i}$, $\sigma_{s\upsilon_i}$, d_{υ_i}, σ_{nt_i}, σ_{st_i}, d_{t_i} noise, scale and length parameters for $\Delta V_{\mathrm{rms}_i}(x_c)$ and $\Delta T_{0_i}(x_c)$, respectively. The multigather case model compensates for lateral variations in the velocity field. Analogous expressions can link the recorded traveltime $\mathcal{T}_i^{(r)}(x, x_c)$ with $V_{\mathrm{int}_{(i)}}(x_c)$ and $\Delta Z_i(x_c)$ allowing probabilistic estimations for all variables of interest in seismic reflection processing.